Revealing the interlayer van der Waals coupling of bi-layer and tri-layer MoS$_2$ using terahertz coherent phonon spectroscopy

Peng-Jui Wang [a], Po-Cheng Tsai [b,c], Zih-Sian Yang [a], Shih-Yen Lin [b,c], Chi-Kuang Sun [a,c,*]

[a] *Department of Electrical Engineering and Graduate Institute of Photonics and Optoelectronics, National Taiwan University, Taipei 10617, Taiwan*
[b] *Graduate Institute of Electronics Engineering, National Taiwan University, No. 1, Section 4, Roosevelt Rd., Taipei 10617, Taiwan*
[c] *Research Center for Applied Sciences, Academia Sinica, 128 Academia Road, Section 2, Nankang, Taipei 11529, Taiwan*

ABSTRACT

In this research, we applied THz coherent phonon spectroscopy to optically probe the vibrational modes of the epitaxially-grown bi-layer and tri-layer MoS$_2$ on sapphire substrate. The layers' THz vibration is displacively stimulated and temporally retrieved by near-UV femtosecond laser pulses, revealing Raman-active and Raman-inactive modes in one measurement. With the complete breathing modes revealed, here we extend the linear chain model by considering the elastic contact with the substrate and vdWs coupling of the next nearest MoS$_2$ layer to analyze the effective spring constants. We further considered the intralayer stiffness as a correction term to acquire the actual interlayer vdWs coupling. Our THz phonon spectroscopy results indicate the interlayer spring constants of 9.03×10^{19} N/m^3 and 9.86×10^{19} N/m^3 for bi-layer and tri-layer respectively. The extended model further suggests that a non-negligible substrate mechanical coupling and next nearest neighbor vdWs coupling of 1.48×10^{19} N/m^3 and 1.04×10^{19} N/m^3 have to be considered.

1. Introduction

Two decades ago, the first isolation of graphene has opened up a wide road toward eventful investigation of two-dimensional materials family [1]. Various 2D materials-based photonics and electronics have been successfully synthesized and fabricated. Among the various choices of 2D materials, the transition metal dichalcogenides (TMDs) are attracting the spot light due to their high on-off ratio [2] and decent carrier mobility [3]. Comparing to graphene, TMDs are more suitable for transistor and visible wavelength optoelectronics applications [4]. However, numerous studies have reported that the interfaces of 2D heterostructures are normally defective, either by intrinsic defects [5], ripples [6], twisted multilayers (in-plane symmetry) [7], or residue trapped inside the interface of the 2D materials [8]. These defects would greatly affect the performance of the 2D based devices [9]. Therefore, techniques for monitoring the quality of 2D structures is in demand for large area growth method of TMDs and the heterostructures.

For the purpose of monitoring the actual interfacial quality after the growing process, Raman spectroscopy is commonly applied to deduce the interlayer [10] and intralayer [11] bonding strength via identification of the vibration modes. The observation of layer breathing (LB) and

shearing (S) modes frequencies within Raman low frequency regime can help to reveal the vdWs bonding by employing the linear chain model [12]. Despite its great success as a molecular analysis tool, this method is inherently limited by the selection rules of active modes, and only the Raman active modes determined by the group theory can be excited [13]. Moreover, the temporal motions of the 2D layers are not time-resolved by Raman spectroscopy. In contrast, ultrafast pump-probe measurement has been widely applied to investigate the femtosecond to nanosecond response of the carrier and quasiparticles dynamics [14–16]. Coherent resonant phonons have been generated and observed by pump-probe in numerous 2D materials, ranging from few layers to bulk types [17]. Sub-terahertz natural resonance has been found in few layer WSe$_2$ and PtSe$_2$, and the calculated interlayer vdWs force constants are 9×10^{19} N/m^3 [18] and $\sim 6 \times 10^{19}$ N/m^3 [19], respectively, which are both lower than graphene of 11×10^{19} N/m^3 [20]. For few layers MoS$_2$, coherent longitudinal acoustic phonon with exfoliated layer number down to 10 layers has been studied [21]. However, interlayer vibrations of bi-layer and tri-layer MoS$_2$ studied by pump-probe techniques and the temporal response have yet to be reported.

In this research, we applied the terahertz photoacoustic spectroscopy to study the sub-picosecond interlayer resonance of the bi-layer and tri-

---

layer MoS$_2$, which were epitaxially grown by sulfurization of the pre-deposited transition metal thin film on a sapphire substrate. The near-UV femtosecond light was focused on the 2D layers to displacively stimulate the out-of-plane vibrations. By removing the carrier dynamics background signal, THz coherent vibration is temporally retrieved by near-UV femtosecond probe pulses. The vdWs force constants correlating to a 1.225 THz resonant frequency of bi-layer MoS$_2$ can be calculated to be 9.03×10^{19} N/m^3 by considering the vdWs coupling to the substrate and the intralayer stiffness coupling. The spring constant connected to substrate is calculated to be 1.48×10^{19} N/m^3. In addition to the 1st breathing mode at 1.010 THz of tri-layer MoS$_2$, we also report the observation of the 2nd breathing mode at 1.545 THz which is inactive by Raman spectroscopy. In the tri-layer case, the mechanical coupling of substrate and next nearest neighbor effect of the 1st and 3rd layer have to be considered following a correction by the intralayer stiffness in order to better fit the experimental results. In this case, the effective spring constants for adjacent layers and the next nearest neighbor layers can be found to be 9.86×10^{19} N/m^3 and 1.04×10^{19} N/m^3 respectively for the first time.

2. Materials and methods

2.1. MoS$_2$ epitaxial growth and characterization

Our large area MoS$_2$ samples were first grown by deposition of nanometer thickness molybdenum films following a sulfurizing process at 850°C. With a sufficient sulfur condition [22], a complete MoS$_2$ film can be obtained on a double side polished sapphire wafer. By fixing the thickness of the Mo film, the layer's number of MoS$_2$ can be precisely controlled [23] with 2H stacking order [24]. This method is known for its uniform and large area sequential growth capable of producing arbitrary heterostructures and also controlling the layer numbers. The cross-sectional high resolution transmission electron microscopy (HRTEM) is applied to determine the actual layer number. As shown in

Fig. 1(a), well arranged crystalline structure was observed and the layer number can be counted to be 2 and 3 respectively. Photoluminescence (PL) spectroscopy and Raman spectroscopy were also employed to confirm the quality of the MoS$_2$ under 532 nm laser excitation. In the Fig. 1(b), the PL spectra for bi-layer and tri-layer MoS$_2$ were acquired under the same system condition. The PL emission peak related to A exciton located at around 678 nm [25] for both samples shows a red-shift comparing to mono-layer MoS$_2$, which is normally 660 nm [26]. The intensity of tri-layer emission is halved compared to that of the bi-layer, resulted from higher degree of indirect bandgap feature [27]. The sharp emission peak at 694 nm is from the sapphire substrate [28]. As shown in Fig. 1(c), two Raman peaks can be observed on the spectra corresponding to intralayer vibration modes E_{2g}^1 and A_{1g}. Wavenumber of E_{2g}^1 and A_{1g} modes are 382.2 cm^{-1} and 403.6 cm^{-1} for the bi-layer, and 382.2 cm^{-1} and 405.6 cm^{-1} for the tri-layer. Increase of the layer number will cause the separation of the two Raman modes [11], which can be corroborated by our measured difference values of the bi-layer (21.4 cm^{-1}) and the tri-layer (23.4 cm^{-1}). After the synthesis and quali-tative measurements, the sample was attached to a hollowed holder in a vacuum chamber for the evacuation with pressure down to 10^{-6} mbar, in order to prevent the oxidation of the MoS$_2$ resulting from the laser illumination.

2.2. Ultrafast pump-probe system

Fig. 1(d) shows a schematic illustration of the THz coherent phonon spectroscopy measurement system [29–31]. Ti:sapphire laser pulses with a 808 nm central wavelength and a 160 fs pulse-width were frequency doubled by a BBO nonlinear crystal. The 404 nm near-UV output was divided by a polarized beam splitter into two beams, which are considered as pump (10 mW) and probe (1 mW) and the pulse-width is 220 fs characterized by an autocorrelator. A motorized stage with retroreflector was used to control the time difference of pump and probe
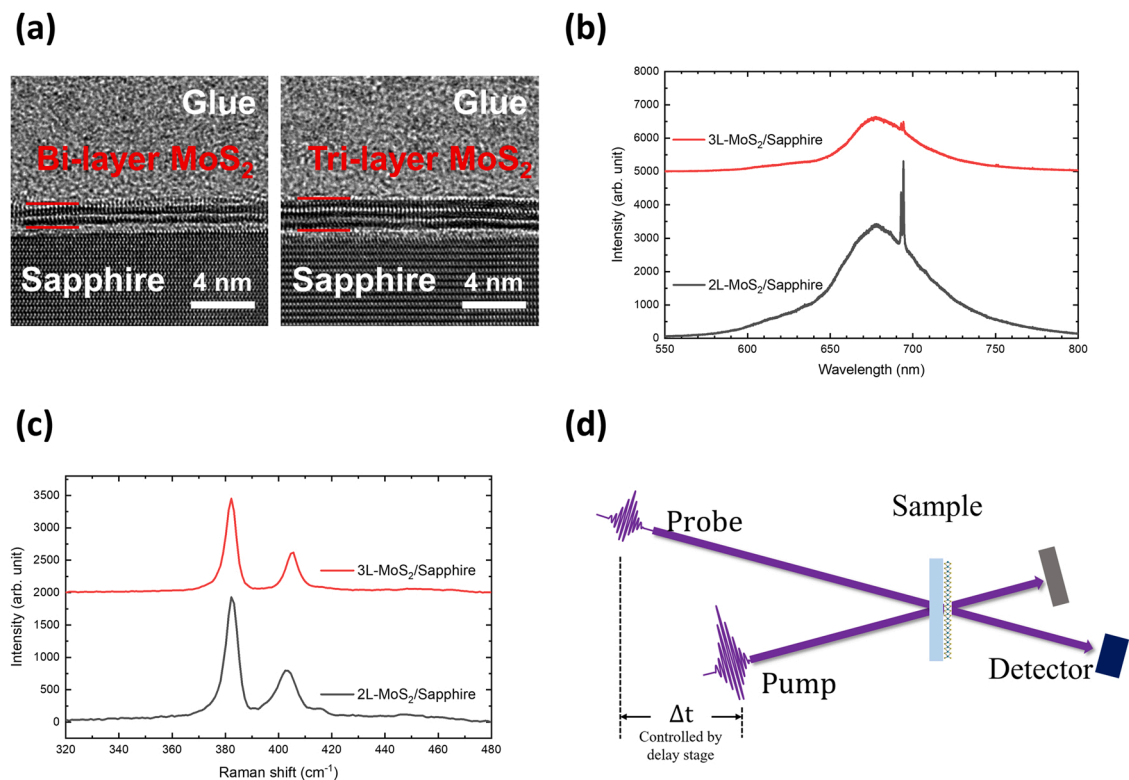

(a)

(b)

(c)

(d)

Fig. 1. (a) HRTEM of the bi-layer and tri-layer MoS$_2$ on Sapphire; (b) PL spectra of bi-layer and tri-layer MoS$_2$ on Sapphire; (c) Raman spectra of bi-layer and tri-layer MoS$_2$ on Sapphire; (d) Schematic illustration of the THz coherent phonon spectroscopy measurement.

pulses. Both beams were later focused by an objective on the MoS_2/Sapphire interface with a ~10 μm spot size, and the maximum pump fluence at the focal point was below 160 μJ/cm^2.

3. Results and discussion

3.1. Carrier dynamics background removal and thus revealed resonance of bi-layer and tri-layer MoS₂

Under the 3.07 eV pump pulse excitation, the carriers were generated well above bandgap in the band-nesting region related to C excitons [32]. Fig. 2(a) shows the relative transmission change (ΔT/T) raw data of both samples, and an abrupt transmission change of the probe light can be observed. The ΔT/T would reach the maximum before 2.1 ps and follow a decaying feature. In our results, the ΔT/T of both samples can be well fitted by a summation of two exponential decays with distinct time constants. The two fitted lifetimes are 8.9 ps and 82.3 ps for the bi-layer MoS_2, and 8.1 ps and 89.5 ps for the tri-layer MoS_2. The time constants are as attributed to a fast decay process from surface state trapping [32], and a relatively slow lifetime resulted from interband recombination and exciton-phonon scattering [33,34]. As the inset of Fig. 2(a) shows, an oscillatory signal can be observed in the residue after removing the fitted exponential decay. Here we used the following target function $\left(\Delta T(t) = a \bullet \left(1 - e^{-\frac{t}{\tau_1}}\right) \bullet \left(e^{-\frac{t}{\tau_2}}\right) + b\right)$ to further remove the background of the residue signal. In Fig. 2(b) we show thus revealed vibrational oscillation signals of the bi-layer and the tri-layer samples respectively. As the near-UV pump pulse excites carriers near the C exciton in MoS_2, energy transfer processes from high energy electrons to lattice would take place immediately. Numerous studies have pointed out that photocarriers on the TMDs lead to the in-plane strain and deformation charge density [35,36], which will thus lead to a new balance state of the lattice positions of the MoS_2 layers. The tendency of moving to the new equilibrium position (minimum of the vdWs potential) would act as a displacive driving force to launch the interlayer coherent vibration, and the natural resonance will be initiated. The relative distance change from the natural resonance of the MoS_2 layers will in turn lead to the variation of the electronic band structure, including the deformation of the valley and the bandgap [37], which will further affect the profile of the refractive index. Therefore, the optical properties such as the light absorption will be modulated as the layers are vibrating, and it provides the main mechanism for the detection of the vibration of the 2D layers via the probe pulse.

Considering the transmission change before ~1 ps is still under the photocarrier transient state, we plotted the retrieved oscillatory traces of the bi-layer and the tri-layer MoS_2 samples from the time when the decaying negative cosinusoidal feature can be recognized. For the bi-layer and the tri-layer MoS_2, the average oscillating periods are 0.8 ps and 1 ps with the first minimum, the starting point of the negative cosinusoidal, extrapolated to be at 0.13 ps and 0.3 ps after time zero, respectively. The femtosecond delay time for the initiation of the displacive oscillation can be attributed to the ultrafast carrier thermalization process usually occurs within tens of femtoseconds. The thermalized photocarriers in the MoS_2 will result in the in-plane compressive strain which has previously been observed and reported in gold nanoparticles on a 2D surface [35], and such strain will also result in the out-of-plane tensile strain. Finally, the vibration amplitude of the tri-layer sample is not monotonically decreasing when compared to the bi-layer sample, a clear indication of multiple frequency interference.

3.2. Spectroscopy study for the layer breathing modes and the deduced vdWs force constants

For the THz spectroscopy study, we applied fast Fourier transform to the time-domain signal to acquire the power spectral density spectra, and we calculated the mean value and the standard error of the mean (SEM) from the distinct points we measured on our samples. The laser spots positions were randomly chosen on samples and the data number for statistics of bi-layer and tri-layer are 9 and 6 respectively. As Fig. 3(a) shows, only one resonant peak of bi-layer sample appears at 1.225 THz with a FWHM bandwidth of 0.290 THz. The SEM value of the central frequency is 0.006 THz. For tri-layer sample, two resonant peaks can be observed with central frequencies at 1.010 THz and 1.545 THz with FWHM bandwidths of 0.280 THz and 0.300 THz respectively. The SEM value of the resonant frequencies are 0.016 THz and 0.005 THz respectively. The peak intensity of the lower frequency mode is about 7.7 times stronger than the higher frequency mode, partially attributed to the limited detection bandwidth of our system. The oscillation's decay time constant can be calculated by (π•FWHM)$^{-1}$, which are 1.10 ± 0.04 ps for all resonances of bi-layer and tri-layer MoS_2.

We first consider the bi-layer MoS_2 resonating without any mechanical coupling to the sapphire substrate. Under this assumption, the resonant frequency can be related to the interlayer effective spring constant (K) by f $= \frac{1}{2\pi}\sqrt{2K/\mu}$, where μ is the area density of monolayer MoS_2 and the factor of 2 inside the square root is resulted from the
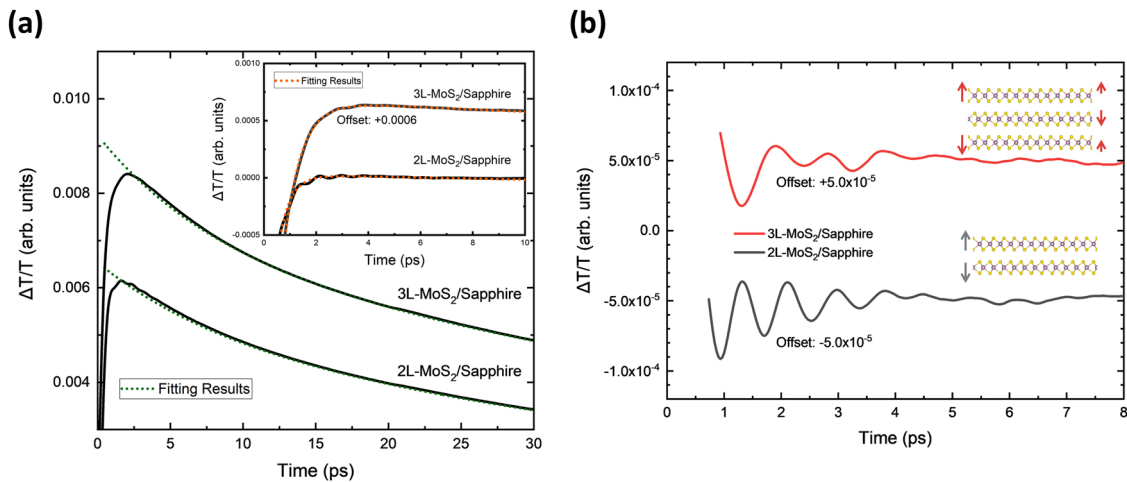

Fig. 2. (a) Illustration of the relative transmission change of bi-layer and tri-layer MoS_2 on sapphire (black solid line) fitted by the exponential decay with two time constants (green dotted line). The inset shows the residue (black solid line) and its fitting results (orange dotted line); (b) The measured interlayer-resonance-induced optical transmission change of bi-layer and tri-layer MoS_2, showing a decaying negative cosinusoidal displacement of the layers. Both traces showed in the figure are single measurements.
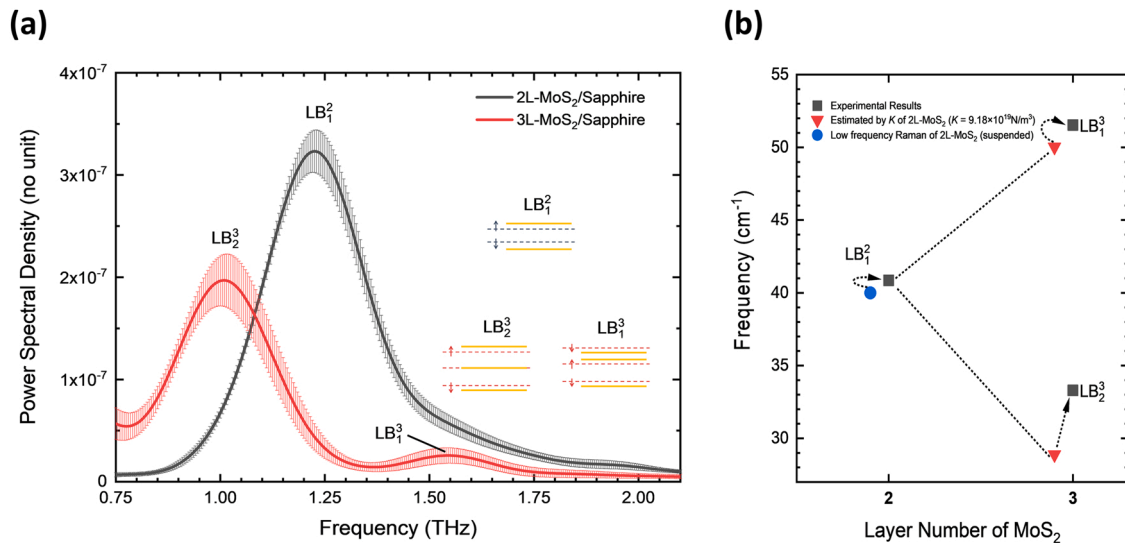
(a)

(b)

Fig. 3. (a) Coherent phonon spectra of the bi-layer (black line) and tri-layer (red line) MoS2 with all corresponding layer breathing modes labeled on the peaks. In the right side of the figure, the layers' displacements (yellow lines) and their equilibrium positions (dashed lines) have been schematic illustrated; (b) The fan diagram of LB modes of bi-layer and tri-layer MoS$_2$ from the experiments, ref [36], and the simple LCM model prediction.

reduced mass of the two-body problem. With the MoS$_2$ area density value of 3.1×10^{-6} kg/m^2 [38] and the average of observed resonant central frequency, the effective spring constant can be calculated as 9.18×10^{19} N/m^3. However, according to the reported low-frequency Raman spectroscopy of few layer suspended 2H-MoS$_2$ by M. O'Brien et al. in 2017 [39], the layer breathing mode is at 40 cm^{-1}, and our experimental measured frequency is corresponding to 40.86 cm^{-1}. The shifted frequency implies that a better model has to be addressed, and it would be discussed in depth in the next section.

Generally, by solving the equation of motion of the linear chain model with N layers of identical 2D films and N-1 identical springs connecting the adjacent layers, the solutions of the resonant frequencies can be written as $f\left(LB_{N,N-j}\right) = \sqrt{2}f\left(LB_{2,1}\right)\sin\left(\frac{j\pi}{2N}\right)$, of which the integer j represents index of the j-th mode and ranges from 1 to (N-1). Therefore, the maximum frequency as the layer number increase would not exceed $\sqrt{2}f\left(LB_{2,1}\right)$, which is 1.732 THz for MoS$_2$ from our experimental results. In addition, the i-th layer's displacement Δr_i^j of the j-th mode can also be calculated to be linearly proportional to $\cos\left[\frac{j(2i-1)\pi}{2N}\right]$. Therefore, the center of the mass remains unchanged during the resonating process around the new equilibrium position.

For the tri-layer MoS$_2$, there are two LB modes denoted as LB$_{3,2}$ and LB$_{3,1}$, and the theoretically estimated resonant frequencies are 0.866 THz and 1.500 THz respectively if we assumed that the force constant of bi-layer MoS$_2$ and tri-layer are identical. Particularly, LB$_{3,2}$: LB$_{2,1}$: LB$_{3,1}$ is $1 : \sqrt{2} : \sqrt{3}$ and LB$_{3,1}$ mode is Raman-inactive but is observable by the ultrafast pump-probe measurement. However, both of our experimentally measured frequencies in the tri-layer are higher than the aforesaid estimation, especially the LB$_{3,2}$ mode with a + 0.144 THz discrepancy (see Fig. 3(b)), which is greater than the SEM value.

3.3. vdWs force constants correction for bi-layer and tri-layer MoS$_2$ by considering the substrate's mechanical coupling and next nearest neighbor effect

The vdWs interlayer coupling force constants are not exactly identical for the samples of distinct layer numbers, especially when the layers are down to few-layer regime. This effect can be observed in the reference [21]. Secondly, the bi-layer and tri-layer MoS$_2$ were epitaxially grown on sapphire substrate and thus the mechanical coupling at the interface would be stronger than the exfoliation samples. There have

been studies [40,41] which report the quantification of the substrate coupling by introducing a force constant in the interface. Moreover, a next nearest neighbour effect has been applied in the study of twisted multilayer graphene to explain the LB modes' difference between theory and experiment [42]. Numerous simulation tools have been developed for the estimation of the potential [43], and the conventional Lennard-Jones potential apparently cannot well-describe those profiles. In order to increase the accuracy of our model, we not only consider the different interlayer force constant values of K_{2L} and K_{3L}, we also consider the vdWs coupling between the 1st and the 3rd MoS$_2$ layers by introducing the K_{13} to represent the long range interaction force constant. We also take K_S to represent the vdWs coupling between the substrate and the 1st epitaxial grown MoS$_2$ layer (see Fig. 4). Since the number of the measured LB modes are three in total, we have to make assumptions to reduce the unknown force constants down to three. Here we considered four cases, which are (1) K_S= 0, (2) K_{13} = 0, (3) K_{2L} = K_{3L}, and (4) K_{2L} acquired from low frequency Raman spectroscopy as a known parameter. Every case is corresponding to two force constant dynamics matrix

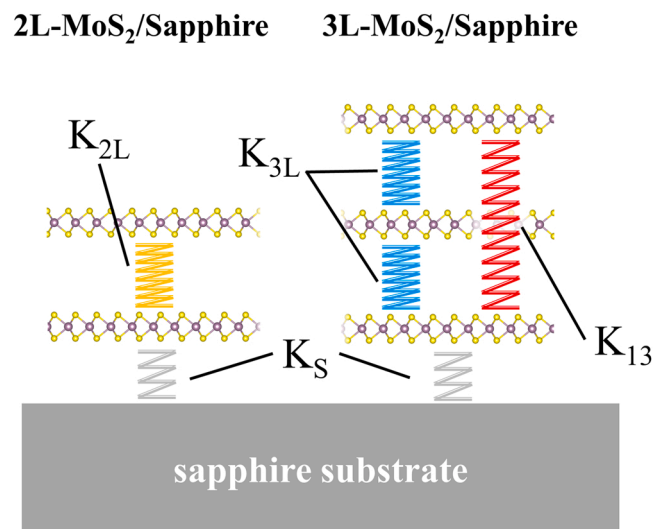**2L-MoS$_2$/Sapphire   3L-MoS$_2$/Sapphire**

Fig. 4. Schematically illustrating the complete models with interlayer vdWs coupling, next nearest neighbour effect, and substrate's mechanical coupling.

Table 1

Dynamics matrix K for bi-layer and tri-layer MoS$_2$ under different constraints so as to limit the number of the unknown force constants. Four cases are discussed, and the fitting results and fitted error show the best-fit force constant values and the sum of the error (%) for the three target frequencies.

#	$\bar{K}$ (2L-MoS$_2$)	$\bar{K}$ (3L-MoS$_2$)	Constraints	Fitting error %	Fitting results ($\div 10^{19}$ N/m^3)
1	$\begin{bmatrix} K_{2L} & -K_{2L} \\ -K_{2L} & K_{2L} \end{bmatrix}$	$\begin{bmatrix} K_{3L}+K_{13} & -K_{3L} & -K_{13} \\ -K_{3L} & 2K_{3L} & -K_{3L} \\ -K_{13} & -K_{3L} & K_{3L}+K_{13} \end{bmatrix}$	$K_S = 0$	0	$K_{2L} = 9.18$ $K_{3L} = 9.74$ $K_{13} = 1.37$
2	$\begin{bmatrix} K_S+K_{2L} & -K_{2L} \\ -K_{2L} & K_{2L} \end{bmatrix}$	$\begin{bmatrix} K_S+K_{3L} & -K_{3L} & 0 \\ -K_{3L} & 2K_{3L} & -K_{3L} \\ 0 & -K_{3L} & K_{3L} \end{bmatrix}$	$K_{13} = 0$	0.58 %	$K_S = 4.72$ $K_{2L} = 7.89$ $K_{3L} = 9.39$
3	$\begin{bmatrix} K_S+K & -K \\ -K & K \end{bmatrix}$	$\begin{bmatrix} K+K_S+K_{13} & -K & -K_{13} \\ -K & 2K & -K \\ -K & -K & K+K_{13} \end{bmatrix}$	$K_{2L} = K_{3L} = K$	2.82 %	$K_S = 0$ $K = 9.25$ $K_{13} = 1.62$
4	$\begin{bmatrix} K_S+K_{2L} & -K_{2L} \\ -K_{2L} & K_{2L} \end{bmatrix}$	$\begin{bmatrix} K_{3L}+K_S+K_{13} & -K_{3L} & -K_{13} \\ -K_{3L} & 2K_{3L} & -K_{3L} \\ -K_{13} & -K_{3L} & K_{3L}+K_{13} \end{bmatrix}$	K_{2L} adopted from ref[39]	0	$K_S = 1.48$ $K_{2L} = 8.80$ $K_{3L} = 9.65$ $K_{13} = 1.04$

$\bar{K}$ for bi-layer and tri-layer MoS$_2$ (see Table 1). We solved the equation of $\bar{K}u = \mu\omega^2 u$, where u is the displacement vector and ω is the angular frequency, and fitted the model to our measured resonant frequencies to find the solution of the unknown force constants.

The fitted solutions of force constants are summarized in the Table 1 and we used $\sum \left| \frac{f_{fitting} - f_{exp}}{f_{exp}} \right|$ to quantify the error between the best-fit results and the experiments. By numerically analysing the effect of the K_S and K_{13}, both of them were found to lead to the increase of the modelled frequencies, thus agreeing with our observations. Specifically, the K_{13} would only affect the lower breathing mode of the tri-layer structure under the substrate-free condition, and non-zero K_S will cause the degenerate branch of the coupled oscillator to reappear again at low frequency regime (tens of GHz). Moreover, the LB modes of 1.225 THz and 1.010 THz for bi-layer and tri-layer are more sensitive to the change of the K_S.

For the 1st case, the substrate was neglected and we saw an increase of the interlayer force constant and a strong next nearest neighbour spring can well-fit the up-shift of the resonance frequencies of tri-layer MoS$_2$. However, this model fails to explain the increase of the LB mode frequency for bi-layer MoS$_2$, which obviously arises from the substrate effect. For the 2nd case, we excluded the next nearest neighbour effect and only considered the substrate effect (K_S) with two distinct interlayer force constant K_{2L} and K_{3L}. The best-fit results bring a 0.58 % total error, and we can see that the fitted substrate effect of 4.72×10^{19} N/m^3 is too large so as to become even greater than the reported interlayer force constants of hBN and InSe [40], which are about 3.7×10^{19} N/m^3 and 4.5×10^{19} N/m^3 respectively. In the 3rd case, we assumed that the interlayer force constant was identical for both bi-layer and tri-layer. However, this model brought an even worse fitting result with a high error of 2.82 % when comparing to previous two cases. Moreover, the K_S tends to be zero in this model, contradicting

the assumption of the non-zero value for the substrate effect.

Finally, we took K_{2L} (8.80×10^{19} N/m^3) as the known factor, which was adopted from previous literatures with free-standing bi-layer MoS$_2$ [39], and utilized the measured 0.86 cm^{-1} resonance frequency difference to estimate our substrate effect. We acquired a value of 1.48×10^{19} N/m^3 for K_S. We then took the K_S into the model of tri-layer with unknown K_{3L} and K_{13} to fit the experimentally measured 1.010 THz and 1.545 THz. The fitting results of $K_{3L} = 9.65 \times 10^{19}$ N/m^3 and $K_{13} = 1.04 \times 10^{19}$ N/m^3 brought a negligible error. We can see that under this model, the substrate coupling effect and the next nearest neighbour effect can both be quantified and we also observed an increase of the force constant as the layer increase from 2 layers to 3 layers, agreeing with the ref [44] for bi-layer and tri-layer suspended 2H-MoSe$_2$ with ~3 % increase. The study of the acoustic parameters for vdWs interfaces of exfoliated hBN and Al film on sapphire substrate from ref [41] gave a range of K_S lower than 10^{19} N/m^3, and our deduced value 1.48×10^{19} N/m^3 is slightly higher, agreeing with the expected higher binding energy between the sapphire and the epitaxial growth of MoS$_2$.

3.4. Intralayer stiffness effect on the net vdWs force constants

We considered that the intralayer of a single MoS$_2$ layer is completely rigid in our previous models. However, the force constant for intralayer covalent bonding is about 2 orders of magnitude greater than that of the interlayer vdWs bonding. A study by W. Yan et al. [45] considered the intralayer covalent bonding springs connecting the rather weak vdWs springs in series, and they used the net springs to estimate the actual force constant in the vdWs gap. Here we followed the same approach and directly took the reported intralayer force constant (K_{2DMs}) of single layer MoS$_2$ to be 6.92×10^{21} N/m^3 [46]. Please refer to Fig. 5(a) for the connected springs in series and this approach was applied to further correct both K_{2L} and next nearest neighbour K_{13}. The relation can be written as effective $K_{2L\ or\ 13} = \left(K_{vdWs}^{-1} + 2K_{2DMs}^{-1} \right)^{-1}$, in which the K_{vdWs}

(a) K_{vdWs} K_{2DMs} K_{2L}

(b) K_{vdWs} K_{2DMs} K_{3L} $\frac{1}{2} K_{3L}$
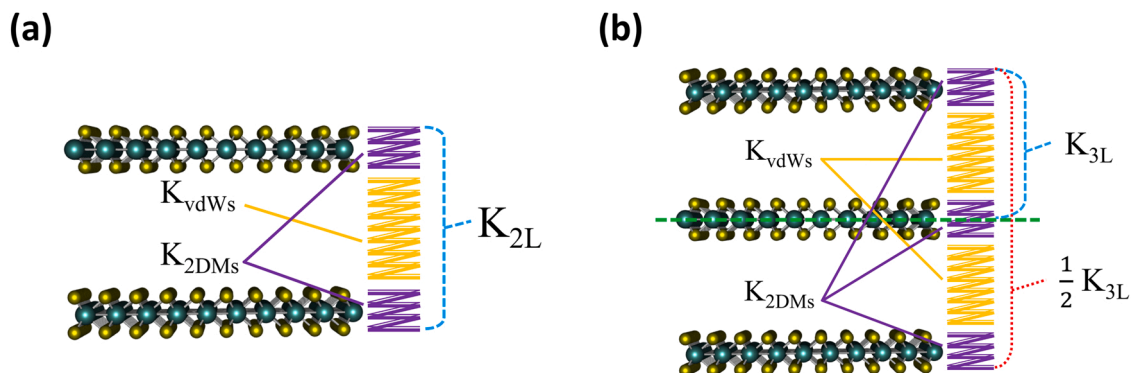
Fig. 5. Schematically illustrating the strong covalent bonding intralayer stiffness connected in series with the force constant for weak vdWs interlayer bonding.

represents the actual vdWs force constant without the effect of intralayer stiffness coupling. Similarly, see Fig. 5(b), the correction relation for interlayer force constant of tri-layer can be written as $K_{3L} = 2\left(2K_{vdWs}^{-1} + 3K_{2DMs}^{-1}\right)^{-1}$.

Here we took the previously acquired effective $(K_{2L}, K_{3L}, K_{13}) = (8.80, 9.65, 1.04) \times 10^{19}$ N/m^3 into the relations, and deduced the corrected interlayer force constants (K_{vdWs}) as 9.03×10^{19} N/m^3, 9.86×10^{19} N/m^3, and 1.04×10^{19} N/m^3 respectively. For the next nearest neighbour effect, our fitted value of K_{13} is about 10 times lower than the interlayer force constant K_{3L}. It is further noted that the interlayer vdWs coupling of few-layer graphene measured by low-frequency Raman spectroscopy has been reported. Comparing to the two corresponding effective spring constants of graphene which are 11.5×10^{19} N/m^3 and 0.93×10^{19} N/m^3 [42] respectively, our results show a similiar next nearest neighbour effect.

4. Conclusion

In conclusion, we used epitaxial growth method to synthesize large area bi-layer and tri-layer MoS$_2$ and optically probed all LB modes of the interlayer vibrations. We identified the resonance peaks from the spectroscopy results. The increase of the LB mode for substrate supported bi-layer MoS$_2$ indicates the mechanical coupling to the substrate has to be considered. The successful observation of the Raman-inactivated mode LB$_{3,1}$ from the tri-layer MoS$_2$ sample can help provide the actual interlayer force constant, including the next nearest neighbour spring constant, and we observe a stronger force constant as the layer number increases from 2 to 3. Our results further suggest that it is insufficient to only consider the linear chain model with an identical effective spring constant of the nearest neighbor. The substrate effect (K_S) and the next nearest neighbor vdWs coupling (K_{13}) have to be taken into account, and both of them are responsible for the correction of the LB$_{3,2}$ mode.

CRediT authorship contribution statement

Peng-Jui Wang: Conceptualization, Methodology, Experiments - ultrafast pump-probe measurements, Validation, Formal analysis, Writing – original draft, Writing – review & editing. **Po-Cheng Tsai**: Experiments - sample growth & sample characterization, Formal analysis, Writing – review & editing. **Zih-Sian Yang**: Experiments - ultrafast pump-probe measurements, Validation, Writing – review & editing. **Shih-Yen Lin**: Formal analysis, Writing – original draft, Writing – review & editing, Supervision. **Chi-Kuang Sun**: Conceptualization, Methodology, Writing – original draft, Writing – review & editing, Supervision, Funding acquisition.

Declaration of Competing Interest

The authors have no conflicts of interest to disclose.

Data Availability

All data has been presented and discussed in the article.

Acknowledgements

References

[1] K.S. Novoselov, A.K. Geim, S.V. Morozov, D. Jiang, Y. Zhang, S.V. Dubonos, I.V. Grigorieva, A.A. Firsov, Electric field effect in atomically thin carbon films, Science 306 (5696) (2004) 666–669.

[2] W. Wu, D. De, S.-C. Chang, Y. Wang, H. Peng, J. Bao, S.-S. Pei, High mobility and high on/off ratio field-effect transistors based on chemical vapor deposited single-crystal MoS2 grains, Appl. Phys. Lett. 102 (14) (2013).

[3] B. Radisavljevic, A. Radenovic, J. Brivio, V. Giacometti, A. Kis, Single-layer MoS2 transistors, Nat. Nanotechnol. 6 (3) (2011) 147–150.

[4] Q.H. Wang, K. Kalantar-Zadeh, A. Kis, J.N. Coleman, M.S. Strano, Electronics and optoelectronics of two-dimensional transition metal dichalcogenides, Nat. Nanotechnol. 7 (11) (2012) 699–712.

[5] W. Zhou, X. Zou, S. Najmaei, Z. Liu, Y. Shi, J. Kong, J. Lou, P.M. Ajayan, B.I. Yakobson, J.C. Idrobo, Intrinsic structural defects in monolayer molybdenum disulfide, Nano Lett. 13 (6) (2013) 2615–2622.

[6] J. Brivio, D.T. Alexander, A. Kis, Ripples and layers in ultrathin MoS2 membranes, Nano Lett. 11 (12) (2011) 5148–5153.

[7] K. Liu, L. Zhang, T. Cao, C. Jin, D. Qiu, Q. Zhou, A. Zettl, P. Yang, S.G. Louie, F. Wang, Evolution of interlayer coupling in twisted molybdenum disulfide bilayers, Nat. Commun. 5 (2014) 4966.

[8] S. Tongay, J. Zhou, C. Ataca, J. Liu, J.S. Kang, T.S. Matthews, L. You, J. Li, J.C. Grossman, J. Wu, Broad-range modulation of light emission in two-dimensional semiconductors by molecular physisorption gating, Nano Lett. 13 (6) (2013) 2831–2836.

[9] S.M. Hus, R. Ge, P.A. Chen, L. Liang, G.E. Donnelly, W. Ko, F. Huang, M.H. Chiang, A.P. Li, D. Akinwande, Observation of single-defect memristor in an MoS2 atomic sheet, Nat. Nanotechnol. 16 (1) (2021) 58–62.

[10] L. Liang, J. Zhang, B.G. Sumpter, Q.H. Tan, P.H. Tan, V. Meunier, Low-frequency shear and layer-breathing modes in Raman scattering of two-dimensional materials, ACS Nano 11 (12) (2017) 11777–11802.

[11] C. Lee, H. Yan, L.E. Brus, T.F. Heinz, J. Hone, S. Ryu, Anomalous lattice vibrations of single- and few-layer MoS2, ACS Nano 4 (5) (2010) 2695–2700.

[12] T.J. Wieting, Long-wavelength lattice vibrations of MoS2 and GaSe, Solid State Commun. 12 (9) (1973) 931–935.

[13] X. Zhang, Q.H. Tan, J.B. Wu, W. Shi, P.H. Tan, Review on the Raman spectroscopy of different types of layered materials, Nanoscale 8 (12) (2016) 6435–6450.

[14] Y.X. Yan, E.B.G. Jr, K.A. Nelson, Impulsive stimulated scattering: general importance in femtosecond laser pulse interactions with matter, and spectroscopic applications, J. Chem. Phys. 83 (11) (1985) 5391–5399.

[15] C.H. Lui, A.J. Frenzel, D.V. Pilon, Y.H. Lee, X. Ling, G.M. Akselrod, J. Kong, N. Gedik, Trion-induced negative photoconductivity in monolayer MoS2, Phys. Rev. Lett. 113 (16) (2014), 166801.

[16] H. Shan, Y. Yu, X. Wang, Y. Luo, S. Zu, B. Du, T. Han, B. Li, Y. Li, J. Wu, F. Lin, K. Shi, B.K. Tay, Z. Liu, X. Zhu, Z. Fang, Direct observation of ultrafast plasmonic hot electron transfer in the strong coupling regime, Light.: Sci. Appl. 8 (1) (2019) 9.

[17] F. Vialla, N. Del Fatti, Time-domain investigations of coherent phonons in van der Waals thin films, Nanomaterials 10 (12) (2020).

[18] T.Y. Jeong, B.M. Jin, S.H. Rhim, L. Debbichi, J. Park, Y.D. Jang, H.R. Lee, D.-H. Chae, D. Lee, Y.-H. Kim, S. Jung, K.J. Yee, Coherent lattice vibrations in mono- and few-layer WSe2, ACS Nano 10 (5) (2016) 5560–5566.

[19] X. Chen, S. Zhang, L. Wang, Y.-F. Huang, H. Liu, J. Huang, N. Dong, W. Liu, I.M. Kislyakov, J.M. Nunzi, L. Zhang, J. Wang, Direct observation of interlayer coherent acoustic phonon dynamics in bilayer and few-layer PtSe2, Photonics Res. 7 (12) (2019).

[20] T. Mishina, K. Nitta, Y. Masumoto, Coherent lattice vibration of interlayer shearing mode of graphite, Phys. Rev. B 62 (4) (2000) 2908–2911.

[21] S. Ge, X. Liu, X. Qiao, Q. Wang, Z. Xu, J. Qiu, P.-H. Tan, J. Zhao, D. Sun, Coherent longitudinal acoustic phonon approaching THz frequency in multilayer molybdenum disulphide, Sci. Rep. 4 (1) (2014) 5722.

[22] C.R. Wu, X.R. Chang, C.H. Wu, S.Y. Lin, The growth mechanism of transition metal dichalcogenides by using sulfurization of pre-deposited transition metals and the 2D crystal hetero-structure establishment, Sci. Rep. 7 (2017) 42146.

[23] C.-R. Wu, X.-R. Chang, T.-W. Chu, H.-A. Chen, C.-H. Wu, S.-Y. Lin, Establishment of 2D crystal heterostructures by sulfurization of sequential transition metal depositions: preparation, characterization, and selective growth, Nano Lett. 16 (11) (2016) 7093–7097.

[24] H.A. Chen, H. Sun, C.R. Wu, Y.X. Wang, P.H. Lee, C.W. Pao, S.Y. Lin, Single-crystal antimonene films prepared by molecular beam epitaxy: selective growth and contact resistance reduction of the 2D material heterostructure, ACS Appl. Mater. Interfaces 10 (17) (2018) 15058–15064.

[25] G.Y. Jia, Y. Liu, J.Y. Gong, D.Y. Lei, D.L. Wang, Z.X. Huang, Excitonic quantum confinement modified optical conductivity of monolayer and few-layered MoS2, J. Mater. Chem. C 4 (37) (2016) 8822–8828.

[26] K.F. Mak, C. Lee, J. Hone, J. Shan, T.F. Heinz, Atomically thin MoS2: a new direct-gap semiconductor, Phys. Rev. Lett. 105 (13) (2010), 136805.

[27] S. Golovynskyi, I. Irfan, M. Bosi, L. Seravalli, O.I. Datsenko, I. Golovynska, B. Li, D. Lin, J. Qu, Exciton and trion in few-layer MoS2: Thickness- and temperature-dependent photoluminescence, Appl. Surf. Sci. 515 (2020).

[28] A. Kostyukov, M. Baronskiy, A. Rastorguev, V. Snytnikov, V. Snytnikov, A. Zhuzhgov, A. Ishchenko, Photoluminescence of Cr3+ in nanostructured Al2O3 synthesized by evaporation using a continuous wave CO2 laser, RSC Adv. 6 (3) (2016), 2072-2078.

[29] C.-K. Sun, Y.-K. Huang, J.-C. Liang, A. Abare, S.P. DenBaars, Coherent optical control of acoustic phonon oscillations in InGaN/GaN multiple-quantum-wells, Appl. Phys. Lett. 78 (9) (2001) 1201–1203.

[30] P.-A. Mante, C.-C. Chen, Y.-C. Wen, H.-Y. Chen, S.-C. Yang, Y.-R. Huang, I.-J. Chen, Y.-W. Chen, V. Gusev, M.-J. Chen, J.-L. Kuo, J.-K. Sheu, C.-K. Sun, Probing hydrophilic interface of solid/liquid-water by nanoultrasonics, Sci. Rep. 4 (2014) 6249.

[31] I.-J. Chen, P.-A. Mante, C.-K. Chang, S.-C. Yang, H.-Y. Chen, Y.-R. Huang, L.-C. Chen, K.-H. Chen, V. Gusev, C.-K. Sun, Graphene to substrate energy transfer through out-of-plane longitudinal acoustic phonons, Nano Lett. 14 (2014) 1317–1323.

[32] H.S. Tsai, Y.H. Huang, P.C. Tsai, Y.J. Chen, H. Ahn, S.Y. Lin, Y.J. Lu, Ultrafast exciton dynamics in scalable monolayer MoS2 synthesized by metal sulfurization, ACS Omega 5 (19) (2020) 10725–10730.

[33] P.D. Cunningham, K.M. McCreary, A.T. Hanbicki, M. Currie, B.T. Jonker, L. M. Hayden, Charge trapping and exciton dynamics in large-area CVD grown MoS2, J. Phys. Chem. C 120 (10) (2016) 5819–5826.

[34] H. Shi, R. Yan, S. Bertolazzi, J. Brivio, B. Gao, A. Kis, D. Jena, H.G. Xing, L. Huang, Exciton dynamics in suspended monolayer and few-layer MoS2 2D crystals, ACS Nano 7 (2) (2013) 1072–1080.

[35] A. Singh, G. Sharma, B.P. Singh, P. Vasa, Charge-induced lattice compression in monolayer MoS2, J. Phys. Chem. C 123 (29) (2019) 17943–17950.

[36] X. Guan, G. Zhu, X. Wei, J. Cao, Tuning the electronic properties of monolayer MoS$_2$, MoSe$_2$ and MoSSe by applying z-axial strain, Chem. Phys. Lett. 730 (2019) 191–197.

[37] J. Xiao, M. Long, X. Li, Q. Zhang, H. Xu, K.S. Chan, Effects of van der Waals interaction and electric field on the electronic structure of bilayer MoS2, J. Phys. Condens Matter 26 (40) (2014), 405302.

[38] M. Li, J. Shi, L. Liu, P. Yu, N. Xi, Y. Wang, Experimental study and modeling of atomic-scale friction in zigzag and armchair lattice orientations of MoS2, Sci. Technol. Adv. Mater. 17 (1) (2016) 189–199.

[39] M. O'Brien, N. Scheuschner, J. Maultzsch, G.S. Duesberg, N. McEvoy, Raman spectroscopy of suspended MoS2, Phys. Status Solidi (B) 254 (11) (2017).

[40] J.D.G. Greener, A.V. Akimov, V.E. Gusev, Z.R. Kudrynskyi, P.H. Beton, Z. D. Kovalyuk, T. Taniguchi, K. Watanabe, A.J. Kent, A. Patanè, Coherent acoustic phonons in van der Waals nanolayers and heterostructures, Phys. Rev. B 98 (7) (2018).

[41] A.Y. Klokov, N.Y. Frolov, A.I. Sharkov, S.N. Nikolaev, M.A. Chernopitssky, S. I. Chentsov, M.V. Pugachev, A.I. Duleba, A.V. Shupletsov, V.S. Krivobok, A. Y. Kuntsevich, 3D hypersound microscopy of van der Waals heterostructures, Nano Lett. 22 (5) (2022) 2070–2076.

[42] J.-B. Wu, Z.-X. Hu, X. Zhang, W.-P. Han, Y. Lu, W. Shi, X.-F. Qiao, M. Ijiäs, S. Milana, W. Ji, A.C. Ferrari, P.-H. Tan, Interface Coupling in twisted multilayer graphene by resonant Raman spectroscopy of layer breathing modes, ACS Nano 9 (7) (2015) 7440–7449.

[43] F.P. Novais Antunes, V.S. Vaiss, S.R. Tavares, R.B. Capaz, A.A. Leitão, Van der Waals interactions and the properties of graphite and 2H-, 3R- and 1T-MoS2: A comparative study, Computational Materials Science 152 (2018) 146–150.

[44] P. Soubelet, A.A. Reynoso, A. Fainstein, K. Nogajewski, M. Potemski, C. Faugeras, A.E. Bruchhausen, The lifetime of interlayer breathing modes of few-layer 2H-MoSe2 membranes, Nanoscale 11 (21) (2019) 10446–10453.

[45] W. Yan, A.V. Akimov, J.A. Page, M.T. Greenaway, A.G. Balanov, A. Patanè, A.J. Kent, Nondestructive Picosecond Ultrasonic Probing of Intralayer and van der Waals Interlayer Bonding in α- and β-In2Se3, Advanced Functional Materials 31 (50) (2021).

[46] X. Zhang, W.P. Han, J.B. Wu, S. Milana, Y. Lu, Q.Q. Li, A.C. Ferrari, P.H. Tan, Raman spectroscopy of shear and layer breathing modes in multilayer MoS2, Phys. Rev. B 87 (11) (2013).

Po-Cheng Tsai received his B.S. degree in optoelectronics from Department of Electro-Optical Engineering National United University, Miaoli, Taiwan, in 2015, and M.S. degree in optoelectronics from Institute of Optoelectronic Sciences, National Taiwan Ocean University, Keelung, Taiwan, in 2017. He is currently studying for Ph.D. degree in Graduate Institute of Electronics Engineering, National Taiwan University, Taipei, Taiwan. His research interests include 2D semiconductors and heterostructure on electrical devices.

Zih-Sian Yang is currently a master degree student of Graduate Institute of Photonics and Optoelectronics in National Taiwan University supervised by Chi-Kuang Sun. He is interested in Terahertz Coherent Phonon Spectroscopy and 2D materials.

Shih-Yen Lin received the Ph.D. degree in electrical engineering from National Taiwan University at 2001. He was the deputy of manager of R&D department at Land Mark optoelectronics corp., Tainan, Taiwan during 2001–2003. From 2003–2006, he was with Electronics & Optoelectronics Research Laboratories, Industrial Technology Research Institute (ITRI), Hsinchu, Taiwan. He joined Research Center for Applied Sciences (RCAS), Academia Sinica, Taipei, Taiwan since 2006. He is now a research fellow at RCAS. His research interests are on the applications of MBE-prepared nano-structures and large-area 2-D crystals for opto-electrical devices. He is now a senior member of IEEE.

Chi-Kuang Sun received his Ph.D. in applied physics from Harvard University in 1995 and was an assistant researcher in the UCSB QUEST Center from 1995 to 1996. In 1996, he joined National Taiwan University, where he is now a distinguished professor of photonics and optoelectronics. He founded the NTU Molecular Imaging Center. His research focuses on nano-acoustics, femtosecond optics, THz optoelectronics, and biomedical imaging. He is a fellow of OSA, SPIE, and IEEE.

Peng-Jui Wang received his B.S. degree in electrical engineering from National Taiwan University in 2014. He is currently a Ph.D. candidate in Graduate Institute of Photonics and Optoelectronics, National Taiwan University. His research focuses on THz photoacoustics, 2D materials, and ultrafast optics.